


RESEARCH ARTICLE | JULY 19 2023

Comparative assessment for pressure field reconstruction based on physics-informed neural network

Di Fan (樊迪) ; Yang Xu (徐杨) ; Hongping Wang (王洪平)  ; Jinjun Wang (王晋军) 



Physics of Fluids 35, 077116 (2023)

<https://doi.org/10.1063/5.0157753>



APL Energy

Latest Articles Online!

[Read Now](#)



Comparative assessment for pressure field reconstruction based on physics-informed neural network

Cite as: Phys. Fluids **35**, 077116 (2023); doi: 10.1063/5.0157753

Submitted: 10 May 2023 · Accepted: 5 July 2023 ·

Published Online: 19 July 2023



View Online



Export Citation



CrossMark

Di Fan (樊迪),¹ Yang Xu (徐杨),¹ Hongping Wang (王洪平),^{2,a)} and Jinjun Wang (王晋军)¹

AFFILIATIONS

¹Fluid Mechanics Key Laboratory of Education Ministry, Beijing University of Aeronautics and Astronautics, Beijing 100191, China

²The State Key Laboratory of Nonlinear Mechanics, Institute of Mechanics, Chinese Academy of Sciences, Beijing 100190, China

^{a)} Author to whom correspondence should be addressed: hpwang@imech.ac.cn

ABSTRACT

In this paper, a physics-informed neural network (PINN) is used to determine pressure fields from the experimentally measured velocity data. As a novel method of data assimilation, PINN can simultaneously optimize velocity and solve pressure by embedding the Navier–Stokes equations into the loss function. The PINN method is compared with two traditional pressure reconstruction algorithms, i.e., spectral decomposition-based fast pressure integration and irrotation correction on pressure gradient and orthogonal-path integration, and its performance is numerically assessed using two kinds of flow motions, namely, Taylor’s decaying vortices and forced isotropic turbulence. In the case of two-dimensional decaying vortices, critical parameters of PINN have been investigated with and without considering measurement errors. Regarding the forced isotropic turbulence, the influence of spatial resolution and out-of-plane motion on pressure reconstruction is assessed. Finally, in an experimental case of a synthetic jet impinging on a solid wall, the PINN is used to determine the pressure from the velocity fields obtained by the planar particle image velocimetry. All results show that the PINN-based pressure reconstruction is superior to other methods even if the velocity fields are significantly contaminated by the measurement errors.

Published under an exclusive license by AIP Publishing. <https://doi.org/10.1063/5.0157753>

I. INTRODUCTION

The flow pressure is an important physical quantity for estimating lift force, drag force (Kurose and Komori, 1999; Saffman, 1965; and Rubinow and Keller, 1961), and acoustics (Bach and Bruus, 2018), which are important for engineering applications (Gunaydinoglu and Kurtulus, 2020). Moreover, unsteady pressure fields play a key role in the evolution and interaction of flow structures (Lee, Ahn, and Sung, 2004 and Voskoboinick, Kornev, and Turnow 2013). Among pressure measurement methods, multiple-hole pitot (Elliott, 1972 and Tsuji *et al.*, 2007) provides only sparse pressure estimation when it is not coupled with the velocity field, and pressure-sensitive paint (McLachlan *et al.*, 1993; Klein *et al.*, 2005; and Kimura *et al.*, 2010) can only obtain surface pressure. These methods cannot meet the requirement of obtaining a three-dimensional high-precision pressure field. Thus, obtaining a pressure field from flow fields, measured with particle image velocimetry (PIV) or particle tracking velocimetry (PTV), has received extensive attention in the field of experimental fluid mechanics (Liu and Katz, 2006 and Cai *et al.*, 2020).

In general, there are two ways to reconstruct pressure fields from velocity fields, i.e., integrating the pressure gradient or solving the pressure Poisson equation (PPE). Regarding the former, the pressure gradient is derived from the Navier–Stokes (N–S) equations, as follows:

$$\nabla p = -\rho \frac{DU}{Dt} + \mu \nabla^2 \mathbf{U}. \quad (1)$$

Here, p is the pressure, \mathbf{U} is the instantaneous velocity field, DU/Dt is material acceleration, and ρ and μ are the density and dynamic viscosity, respectively. Material acceleration can be calculated using the Eulerian or Lagrangian method, as presented by Liu and Katz (2006). Then, the pressure is computed by integrating the pressure gradient along a specified path. Pressure reconstruction is sensitive to many factors, including the velocity noise (McClure and Yarusevych, 2017; de Kat and van Oudheusden, 2012; Pan *et al.*, 2016; and Liu and Moreto, 2020), boundary condition setup (Faiella *et al.*, 2021), numerical method (Nie *et al.*, 2022), spatial and temporal resolutions (Nie *et al.*, 2022; Charonko *et al.*, 2010; and van Oudheusden, 2013), and error

profile (Faiella *et al.*, 2021). To further improve the quality of pressure reconstruction, Liu and Katz (2006) developed an omni-directional integral algorithm with a virtual boundary (VB-ODI) to average the pressure from all paths. Although this strategy can reduce the dependence on the integral path and the effect of measurement noise, it also leads to low efficiency and high complexity. Moreto *et al.* (2022) adopted a parallel-ray omni-directional integration algorithm to construct a three-dimensional time-averaged pressure field over streambeds. The mean error of pressure was three orders of magnitude smaller than that of the reconstructed pressure value. To further reduce the number of integral paths and improve calculation efficiency, Dabiri *et al.* (2014) developed an eight-path integration method (EPI) using eight families of integration paths, with each family originating at the domain boundary and propagating toward each grid point from the left, upper left, top, upper right, right, lower right, bottom, and lower left. EPI is faster than VB-ODI because it only integrates pressure along eight fixed paths, a much smaller number of paths than that used in VB-ODI. Nevertheless, it is difficult to achieve satisfactory accuracy, particularly when applied to a three-dimensional flow case. Wang *et al.* (2016) developed an irrotation correction on pressure gradient and orthogonal-path integration method (IC-OPI) to reconstruct the pressure field. After the irrotation correction of the pressure gradient, the dependence of the pressure calculation on integral paths could be removed. Then, the pressure was reconstructed from integration along two orthogonal paths, which significantly reduced the computation time without sacrificing the accuracy.

Another means of obtaining the pressure field is to solve the PPE. Applying divergence to both sides of Eq. (1) and assuming that the velocity is incompressible, the PPE is expressed as

$$\nabla^2 p = \nabla \cdot \left[-\rho \frac{D\mathbf{U}}{Dt} + \mu \nabla^2 \mathbf{U} \right]. \quad (2)$$

Fujisawa *et al.* (2006) evaluated pressure fields in a microchannel flow from the measured velocity by solving the PPE. The calculated pressure was in good agreement with the numerical simulation. However, velocity noise had a negative effect on the pressure reconstruction; for example, the pressure error was approximately 2.5% when the velocity noise was 4.3% in their experiment. To improve the accuracy and efficiency of solving PPE, Wang *et al.* (2017) proposed a spectral decomposition-based fast pressure integration (SDFPI) algorithm. Because it seeks the least square solution for the discrete momentum conservation equation by matrix decompositions, SDFPI overcomes the issue of periodical boundaries that occur in the FFT method and could accurately reconstruct the pressure from a pressure gradient. In this paper, SDFPI is adopted as an improved PPE method for comparison with physics-informed neural network (PINN)-based pressure reconstruction. Cai *et al.* (2020) proposed a variational method with a smoothness constraint to extract pressure from two-dimensional velocity field. This method is more robust against velocity errors, and the reconstructed pressure fields can reveal correlation between the low-pressure regions and the vortical structures in a simulated two-dimensional oblique Hiemenz flow. In another study, Zhang, Bhattacharya, and Vlachos (2022) estimated the error and uncertainty of pressure field reconstructed by PPE for a two-dimensional pulsatile channel flow. By adding various levels of artificial noise, a pressure field was reconstructed by solving an overdetermined system involving

pressure gradient error, and this method can improve the accuracy of pressure reconstruction using uncertainty information.

Recently, a physics-informed neural network (PINN) has been used to solve forward and inverse problems involving nonlinear partial differential equations (Raissi, Perdikaris, and Karniadakis, 2017a; Raissi, Perdikaris, and Karniadakis, 2017b; and Raissi, Perdikaris, and Karniadakis, 2019). By combining physical and mathematical understanding with a pure data-driven neural network (Karniadakis *et al.*, 2021), PINN can improve both the interpretability and prediction accuracy of traditional neural networks. PINN does not possess an advantage in directly solving partial differential equations comparing with conventional numerical methods in terms of efficiency and precision, but they have performed well in data assimilation by combining laws of physics (such as the N-S equations) with observed data. Thus, PINN has received widespread attention. For example, incorporating point kinetics equations, a single-layer PINN has been trained to achieve a high computational performance in nuclear reactor dynamics (Schiassi *et al.*, 2022). Wu *et al.* (2022) combined the standard nonlinear Schrödinger equation in PINN to predict the dispersion and nonlinearity coefficients of optical soliton solutions. By combining the heat transfer law in PINN for direct energy deposition processes, a three-dimensional temperature field was predicted with a 4.83% mean temperature relative error (Xie *et al.*, 2022).

For fluid mechanics, Raissi, Yazdani, and Karniadakis (2020) developed a physics-informed deep-learning framework by encoding the N-S equations into neural networks to infer velocity and pressure fields from flow visualizations. Mao, Jagtap, and Karniadakis (2020) adopted PINN to approximate the Euler equations in the compressible flow and solve inverse problems that cannot even be solved using standard techniques. PINN can be also used in one-dimensional advection flow (Vadyala, Betgeri, and Betgeri, 2022), which has the ability to avoid the inaccuracy and computational uncertainty associated with the pseudo-diffusive effect of the conventional method. Arzani, Wang, and D'Souza (2021) showed that PINN could use sparse two- or three-dimensional velocity measurements away from the wall to quantify wall shear stress, leading to very high accuracy, even without full knowledge of the boundary conditions in near-wall flow. The Cahn-Hilliard equation and N-S equations are encoded into the loss of PINN to simulate two-dimensional incompressible two-phase flow (Qiu *et al.*, 2022). The results indicate that PINN is adequate to describe bubble dynamics and to deal with a two-phase flow at the large density ratio. The dense velocity fields reconstructed using PINN from the data of PIV or PTV show that PINN is a useful tool for optimizing measured data and predicting unknown quantities (Wang, Liu, and Wang, 2022). Calicchia *et al.* (2023) used a PINN to accurately predict the pressure field near and on the fish's body, and they found that PINN is insensitive to the spatiotemporal resolution of the PIV measurements. Du *et al.* (2023) imposed nondimensional N-S equations in the loss function of PINN to estimate intra-vascular pressure, which showed the potential of PINN in the cardiovascular disease diagnosis. From their results, PINN can be used to infer the pressure fields without solving the PPE or integrating the pressure gradient. Therefore, the development of the neural network provides an alternative approach to solve pressure fields.

The objective of the present work is to reconstruct the pressure field using PINN from the velocity measured by PIV and quantify the performance of PINN-based pressure reconstruction by comparing

with the other two algorithms, i.e., SDFPI (Wang *et al.*, 2017) and IC-OPI (Wang *et al.*, 2016). Two numerical cases and one experimental case are used to evaluate the performance of PINN. Specifically, the two numerical cases are two-dimensional Taylor’s decaying vortices and forced isotropic turbulence, and the experimental case is a synthetic jet impinging on the solid wall. The remainder of this paper is organized as follows. In Sec. II, the principles of PINN-based pressure reconstruction are introduced. Section III presents our results and discussion. In Sec. III A, the performance of PINN-based pressure reconstruction for different neural network parameters is tested with and without velocity measurement noise. In Sec. III B, we use direct numerical simulation (DNS) data on forced isotropic turbulence to assess the impact of flow three-dimensionality and velocity resolution on the present method. In Sec. III C, we apply the proposed method to a planar PIV for an impinging synthetic jet. Section IV provides our conclusion and thoughts on the potential of PINN in pressure reconstruction.

II. PINN-BASED PRESSURE RECONSTRUCTION

In this section, the basic idea and theory of reconstructing the pressure field using PINN are introduced. Although Wang, Liu, and Wang (2022) had presented examples to obtain the flow pressure from PINN, their study focused on the use of PINN to reduce velocity noise and did not involve an in-depth analysis on the pressure reconstruction. Figure 1 shows the adopted PINN architecture to reconstruct the pressure fields in the current study. A residual neural network is built to fit the relationship between inputs and outputs, which can be expressed as

$$(\mathbf{U}, p) = R_{NN}(\mathbf{X}, t; \Theta). \tag{3}$$

Here, R_{NN} represents the neural network, whose inputs are the spatial coordinates $\mathbf{X} = (x, y, z)$ and time t , and the parameter Θ represents the trainable variables. The outputs of the neural network are velocity vector $\mathbf{U} = (u, v, w)$ and pressure p .

After creating the neural network, the partial derivatives including $\partial\mathbf{U}/\partial\mathbf{X}$, $\partial\mathbf{U}/\partial t$, $\partial p/\partial\mathbf{X}$, $\partial^2\mathbf{U}/\partial\mathbf{X}^2$ used in N-S equations are constructed from the chain rule by using the automatic differentiation. The residuals of the three-dimensional N-S equations can be expressed in the network as follows:

$$\begin{aligned} e_{1,2,3} &= \frac{\partial\mathbf{U}}{\partial t} + (\mathbf{U} \cdot \nabla)\mathbf{U} + \nabla p - \frac{1}{Re}(\nabla^2\mathbf{U}), \\ e_4 &= \nabla \cdot \mathbf{U}, \end{aligned} \tag{4}$$

where Re represents the Reynolds number; e_1 , e_2 , and e_3 are residuals of momentum equation in the x , y , and z directions, respectively; and e_4 is the residual of continuity equation. Within the PINN, the N-S equations are solved by minimizing the equation residuals. Only two-dimensional N-S equations are needed for the two-dimensional cases. To optimize this network, the total loss is defined as $E = E_{data} + \alpha E_{eqns}$, where α is the weighting coefficient for combining the data loss E_{data} and N-S equations loss E_{eqns}

$$E_{data} = \sum_{j=1}^{N_{data}} \left| \mathbf{U}_{input}(\mathbf{X}^j, t^j) - \mathbf{U}_{pred}(\mathbf{X}^j, t^j) \right|^2, \tag{5}$$

$$E_{eqns} = \sum_{i=1}^4 \sum_{j=1}^{N_{eqns}} \left| e_i(\mathbf{X}^j, t^j) \right|^2. \tag{6}$$

Here, E_{data} represents the data loss between the input velocity data \mathbf{U}_{input} and the velocity predicted by the network \mathbf{U}_{pred} . E_{eqns} represents the residual of the N-S equations, including e_1 , e_2 , e_3 , and e_4 . The parameters N_{data} and N_{eqns} are the numbers of data points and equation points. The points are randomly selected and uniformly distributed across the computational domain. According to the results of Wang, Liu, and Wang (2022), increasing weighting coefficient α could enhance the constraint of N-S equations, but it cannot improve the accuracy of the PINN. Thus, following Wang, Liu, and Wang (2022), α is chosen as 1 in the current study to achieve the best performance for the pressure reconstruction.

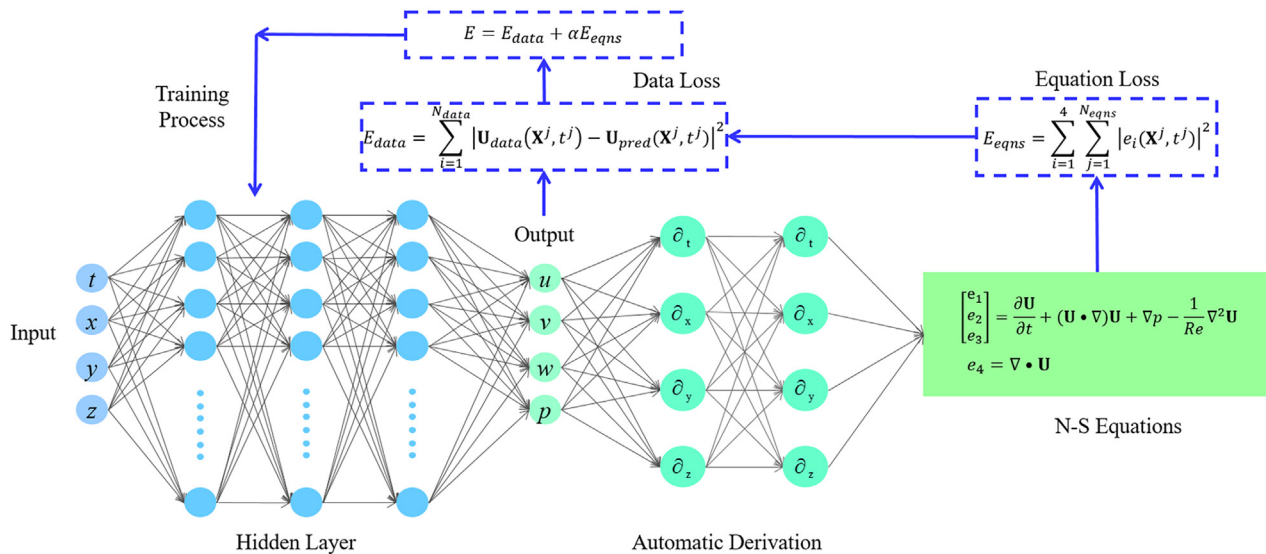


FIG. 1. Schematic of PINN for incompressible N-S equations in the present study.

For neural network, N_{layer} and N_{cell} are used to denote the number of hidden layers and the number of neurons in each hidden layer, respectively. The learning rate is set to exponentially decay in a staircase manner, and the network is trained for 10 000 epochs with 10 steps per epoch unless otherwise specified. The PINN program is coded on the open-source machine learning platform TensorFlow v2.1.0 within Python. The training and test process are conducted on a workstation equipped with a single NVIDIA Quadro RTX 5000 GPU with memory of 16 GB. Additionally, the codes of SDFPI and IC-OPI in this study can be found in Wang *et al.* (2017) and Wang *et al.* (2016), respectively.

III. RESULTS AND DISCUSSION

To comprehensively examine the performance of PINN in the reconstruction of pressure, two numerical cases and one experimental case are tested in this work. First, a two-dimensional flow with a theoretical solution is selected to generate accurate velocity fields. By adding artificial noise of different levels to the velocity fields, the PINN-based pressure reconstruction is compared to the other methods in terms of robustness and accuracy. Second, the forced isotropic turbulence is used to figure out whether PINN can infer three-dimensional pressure from a two-dimensional measurement. In addition to the comparison of reconstructed pressure among different methods, the influence of velocity spatial resolution on the pressure reconstruction is also discussed in this case. Finally, an experimental case of impinging synthetic jets is tested to demonstrate the performance of PINN for real experimental data.

Actually, all the methods, including PINN, IC-OPI, and SDFPI, need to specify a reference pressure to completely determine the values of whole pressure field. Therefore, in the current study, all constructed pressure fields shown in Sec. III are subtracted from their average value at each time instant to minimize the uncertainty caused by the choice of the reference pressure or background pressure. In addition, for the IC-OPI method, the starting point of the pressure gradient integration is selected at the left-bottom corner of the flow field (Wang *et al.*, 2016). While for the SDFPI method, following Wang *et al.* (2017), the pressure Poisson equation is solved with the Neumann boundary condition, which is derived by applying Navier–Stokes (N–S) equations to the boundary of the solution domain.

A. Two-dimensional Taylor’s decaying vortices

In this numerical flow case, two-dimensional Taylor’s decaying vortices with a theoretical solution are employed to validate the performance of pressure reconstruction among different methods. The two-dimensional solution to the incompressible N–S equations at $Re = 1$ is expressed as follows (Kim and Moin, 1985 and Ethier and Steinman, 1994):

$$\begin{cases} u(x, y, t) = -\cos(x)\sin(y)e^{-2t}, \\ v(x, y, t) = \sin(x)\cos(y)e^{-2t}, \\ p(x, y, t) = -\frac{1}{4}(\cos(2x) + \cos(2y))e^{-4t}. \end{cases} \quad (7)$$

Here, t is time, p is pressure, u is the velocity component in the x direction, and v is the velocity component in the y direction. The size of the computation domain is set as $(L_x, L_y, L_t) = (2\pi, 2\pi, 1)$, and the number

of grid points is $(N_x, N_y, N_t) = (100, 100, 100)$, which are uniformly distributed along their directions.

In real experiments, velocity data are always contaminated by the measurement noise. Thus, it is important to evaluate the influence of velocity noise on the performance of the pressure reconstruction method. In this study, Gaussian white noise is added to the theoretical velocity fields to simulate the measurement noise in experimental measurements. The noise level σ varies from 0% to 25% and is defined as the ratio of the standard deviation of the random noise to the velocity fluctuation. When σ reaches 10%, the signal-to-noise ratio (SNR) decreases to 19.8 dB, where $SNR = 10 \log_{10}(P_s/P_n)$ dB, P_s represents the overall sum of the theoretical velocity values squared across the entire field, and P_n denotes the sum of squared velocity noise values across the same field.

Figures 2(a)–2(c) show pressure fields reconstructed using the SDFPI, IC-OPI, and PINN methods, respectively. In addition, the pressure fields calculated using PINN-SDFPI and PINN-IC-OPI are also presented for comparison, as shown in Figs. 2(d) and 2(e). PINN-SDFPI and PINN-IC-OPI mean that the pressure is calculated using SDFPI and IC-OPI from velocity fields optimized by PINN. When the velocity field is not contaminated, i.e., where the noise level $\sigma = 0$, the pressure fields reconstructed by all methods are consistent with the theoretical solution expressed in Eq. (7). As the noise level increases, reaching 5% and 10%, the SDFPI and IC-OPI method are almost incapable of reconstructing the pressure, the results are significantly contaminated by the noise. For the PINN, the level of noise has a little effect on the reconstructed pressure (Fig. 2). It is clear that both SDFPI and IC-OPI are quite sensitive to velocity noise, which can be attributed to the error amplification when computing the material derivative. Nevertheless, the pressure reconstruction performances of SDFPI and IC-OPI were significantly improved in dealing with the optimized velocity by PINN. Therefore, it can be concluded that PINN-based pressure reconstruction is superior to other methods due to the fact that PINN has the capability to optimize the velocity.

For a more quantitative analysis of the accuracy of the reconstructed pressure field, the relative L^2 norm error of p is expressed as follows:

$$\delta_p = \frac{\|p_p - p_e\|_2}{\|p_{ref}\|_2}. \quad (8)$$

Here, the subscripts $(\cdot)_e$, $(\cdot)_p$, and $(\cdot)_{ref}$ represent the exact, predicted, and reference values, respectively. Notably, the reference value is selected to be equivalent to the exact value. Figure 3 quantitatively presents the influence of velocity measurement noise on the predicted pressure field. The noise level σ of the velocity field varies from 0% to 25%, and five methods are compared, namely, PINN, SDFPI, IC-OPI, PINN-SDFPI, and PINN-IC-OPI. The IC-OPI method has the largest relative L^2 norm pressure error, with SDFPI following as the second largest. With increasing velocity noise level, δ_p increases linearly across the two methods. δ_p rapidly increases to about 3621% as velocity noise level increases from 0% to 25% for the IC-OPI method, and δ_p increases to about 3146% for the SDFPI method. These two methods are sensitive to velocity noise, and relative L^2 norm pressure error is much larger than relative L^2 norm velocity error. When the PIV measurement has large noise, the pressure field cannot be satisfactorily reconstructed by these two methods. Figure 3(b) also displays the δ_p of the other three methods. After dealt with PINN, the δ_p increases to

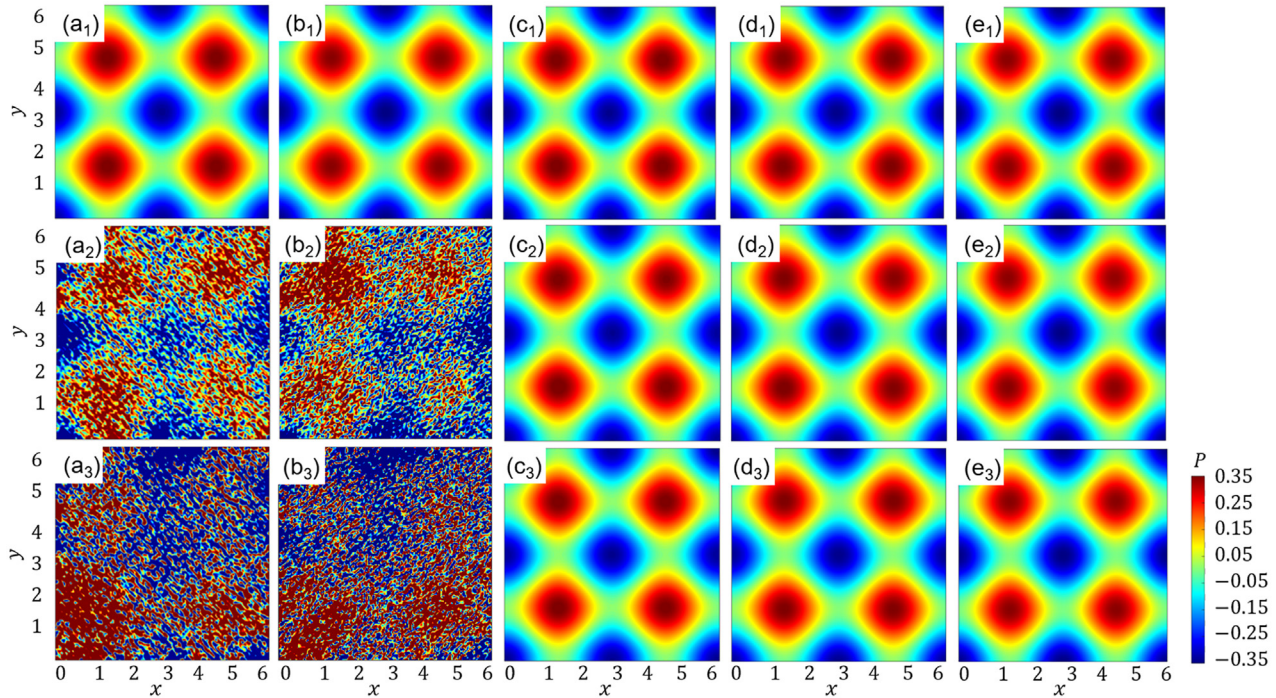


FIG. 2. Contours of pressure predicted by (a) SDFPI, (b) IC-OPI, (c) PINN, (d) PINN-SDFPI, and (e) PINN-IC-OPI. Input velocity has (a₁)–(e₁) 0% noise, (a₂)–(e₂) 5% noise, and (a₃)–(e₃) 10% noise. In PINN, N_{cell} and N_{layer} are 64 and 7, N_{eqns} and N_{data} are 10 000 and 100 000 for all cases, and the time instant is $t = 0.1$.

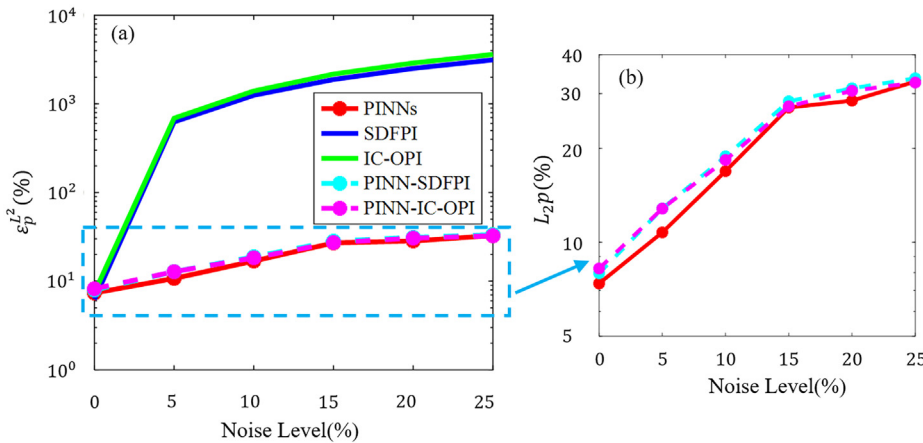


FIG. 3. Charts of the relative L^2 norm error of pressure estimated using (a) SDFPI, IC-OPI, PINN, PINN-SDFPI, and PINN-IC-OPI, and (b) amplification of pressure estimated using the last three methods. The figure is presented using logarithmic scale for the y axis. The Gaussian random noise of the velocity fluctuation ranges from 0% to 25% at an interval of 5%. For PINN, N_{cell} is 64, N_{layer} is 7, N_{eqns} and N_{data} are fixed to 10 000 and 100 000, respectively, and training is conducted for 10 000 epochs.

~30% when the noise level increases to 25%, which exhibits a significant reduction compared to the SDFPI and IC-OPI methods. Elevations in velocity noise level result in gradual increments of δ_p , and the relative pressure errors of all the PINN-related methods (PINN, PINN-SDFPI, and PINN-IC-OPI) present good consistency in the test range. For traditional methods, if the pressure field is reconstructed using the velocity field optimized by PINN, the relative L^2 norm error of pressure is much lower than that calculated directly. Therefore, when measured PIV data are of poor quality and contaminated by noise, PINN can greatly help to improve the quality of velocity and pressure.

In the previous analyses, the performance of PINN is superior to that of SDFPI and IC-OPI due to the physical constraints imposed by the network. To take full advantage of PINN, it is necessary to further evaluate the effects of the number of data points and equation points on the performance of PINN. Figure 4 displays the relative L^2 norm error of pressure as a function of N_{eqns} and N_{data} . The noise level is 0%, 5%, and 10%, the number of data points and equation points vary from 100 to 100 000 and 10 to 10 000, respectively. N_{data} cannot be set to 0 because training the neural network without data points is not feasible. The neural network has seven layers with 64 neurons in each layer, and the learning rate is step decreased at an initial learning rate of 0.01.

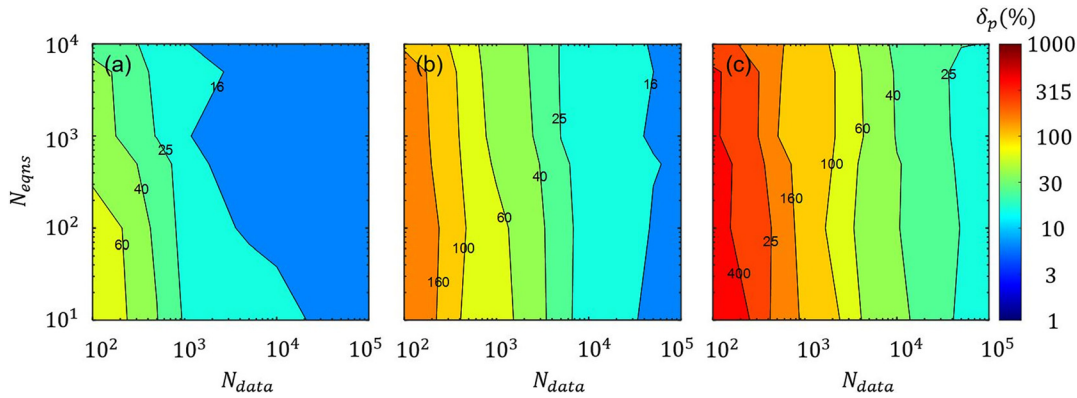


FIG. 4. Contour maps of the relative L^2 norm error of pressure as a function of N_{eqns} and N_{data} . The figure is presented using logarithmic axes. Gaussian random noise with (a) 0%, (b) 5%, and (c) 10% of the velocity fluctuation is added to the velocity. The number of data points varies from 10^2 to 10^5 , and the equation points number varies from 10 to 10^4 . There are 64 neurons in each layer, and the number of layers is set to 7. The training is conducted for at least 10 000 epochs to make sure that the total loss converges in all cases.

In general, with an increase in N_{data} and N_{eqns} , especially for N_{data} , the performance of neural network will be better and δ_p decreases. For different noise levels, increasing the number of equation points has limited influence on the accuracy of pressure field. At a specific N_{eqns} , the relative L^2 norm pressure error presents an evident decreasing trend with an increase in N_{data} . Even the noise level σ is set to 10%, δ_p can finally converge to approximately 20%. Increasing N_{data} can reduce the relative L^2 norm pressure error of the predicted pressure field; therefore, training PINN with more data points is a wise choice.

The influence of the number of data points and the number of neurons in each layer on the performance of the PINN is also evaluated at a velocity noise level of 0%, 5%, and 10%. Figure 5 shows relative L^2 norm error of pressure as a function of N_{data} and N_{cell} . The parameter N_{cell} increases from 16 to 64, which means that the scale of neural increases from small to large. Generally, δ_p decreases with an increase in N_{data} and N_{cell} , even if training velocity data have different noise levels. When the input velocity is an exact N-S equations solution without measurement noise, as shown in Fig. 5(a), δ_p converges to approximately 12%, 8%, and 4% at $N_{cell} = 16, 32,$ and 64, respectively. For pressure, when input velocity noise increases to 10%, δ_p converges to approximately 50%, 26%, and 24% at $N_{cell} = 16, 32,$ and 64 when N_{data} is larger than 50 000.

Based on the tests of the two-dimensional Taylor’s decaying vortices, there are some remarks those can be provided. In general, relative L^2 norm pressure error decreases with an increase in N_{data} . Increasing the scale of the network (represented by N_{cell}) can also reduce the relative L^2 norm pressure error of the predicted pressure field, but this works only when the PINN is fed sufficient data. The relative L^2 norm error of pressure increases with increasing noise level, which implies that the measurement noise of the PIV indeed deteriorates the performance of the PINN; however, the PINN can reduce the influence of velocity noise on pressure estimation. The choice of parameters in later sections is based on the conclusions in this section.

B. Forced isotropic turbulence

Two-dimensional forced homogeneous isotropic turbulence is chosen as the second case to assess the impact of the third component on the pressure reconstruction. This implies that two training data sets are generated to mimic the 2D2C PIV fields and 2D3C PIV fields. The original DNS data set of forced isotropic turbulence on a 1024^3 periodic grid in a cubic domain with a length of 2π is downloaded from the Johns Hopkins Turbulence Databases (Li et al., 2008). The data set includes all the three components of the velocity vector and the pressure.

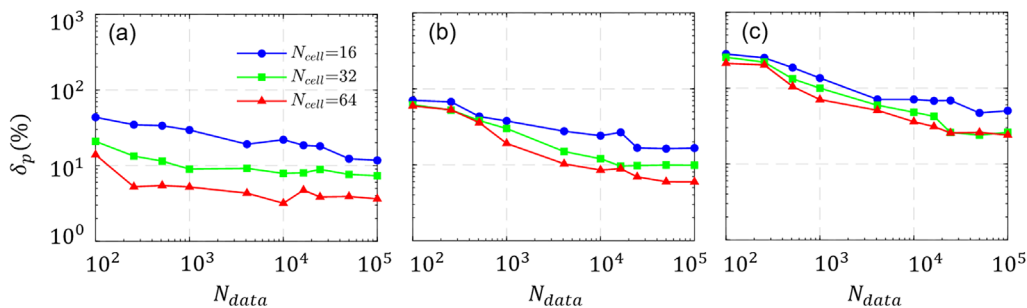


FIG. 5. Relative L^2 norm error of pressure vs N_{data} , N_{cell} , and velocity noise. The figure is presented using logarithmic axes. Gaussian random noise of (a) 0%, (b) 5%, and (c) 10% of the velocity fluctuation is added to the velocity. N_{cell} is chosen as 16, 32, and 64. N_{layer} is fixed to 7, N_{eqns} is fixed to 10 000, and training is conducted for 10 000 epochs in all cases.

TABLE I. Parameters of the forced isotropic turbulence.

Resolution, N	1024
Time step of DNS, Δt	0.0002
Time interval between stored data sets, δt	0.002
Total kinetic energy, $E_{tot} = \frac{1}{2} u_i u_i$	0.695
Dissipation, $\varepsilon = 2\nu S_{ij} S_{ij}$	0.0928
Kolmogorov timescale, $\tau_\eta = \sqrt{\frac{\nu}{\varepsilon}}$	0.0424
Kolmogorov length scale, $\eta = \nu^{3/4} \varepsilon^{-1/4}$	0.0028

The simulation time step Δt is 0.0002. The data are stored at every 10 DNS time steps so the samples are stored at time step $\delta t = 0.002$. The total kinetic energy and dissipation rate are computed by averaging the time between $t = 0$ and $t = 10$. The parameters of the data set are given in Table I.

To simulate the 2D2C PIV velocity fields, 500 two-dimensional x - y slices of two-component velocity data are used to generate particle image pairs, and an FFT-based cross correlation method is used to calculate the velocity from the particle image pairs. The particle image resolution is set to 1024×1024 pixels with a digital imaging resolution of $0.2 \eta/\text{pixel}$. The particles per pixel (ppp) is set to 0.1, and the particle diameter d_p is set to 1.5 pixels. During particle image pairs generation process, mesh and velocity are first non-dimensionalized using Kolmogorov length scale η and timescale τ_η . Then, velocity is computed using mainstream FFT-based cross correlation PIV method based on the generated particle image pairs. The interrogation window is 16×16 pixels with 50% overlap. The vector fields are smoothed using a standard 3×3 local median filter. The resolution of the resulting vector fields, as given by the interrogation window size, is about $3 \eta \times 3 \eta$ (Cai et al., 2020; Buxton, Laizet, and Ganapathisubramani, 2011; and van Gent et al., 2017), adjacent vectors are separated by 1.5η , and the total vector size is 137×137 . For PINN, the network with $N_{layer} = 15$ and $N_{cell} = 128$ is trained by using 10^5 data points and 10^4 equations points. The training process stops after 20 000 epochs, for a total of about 28 h, with a learning rate that exponentially decays from 0.01 in a staircase manner. The loss as a function of the number of epochs converges from about 20 to about 0.1.

Figure 6 shows the original DNS data and the pressure field calculated by SDFPI, IC-OPI, and 2 D PINN at the 100th snapshot.

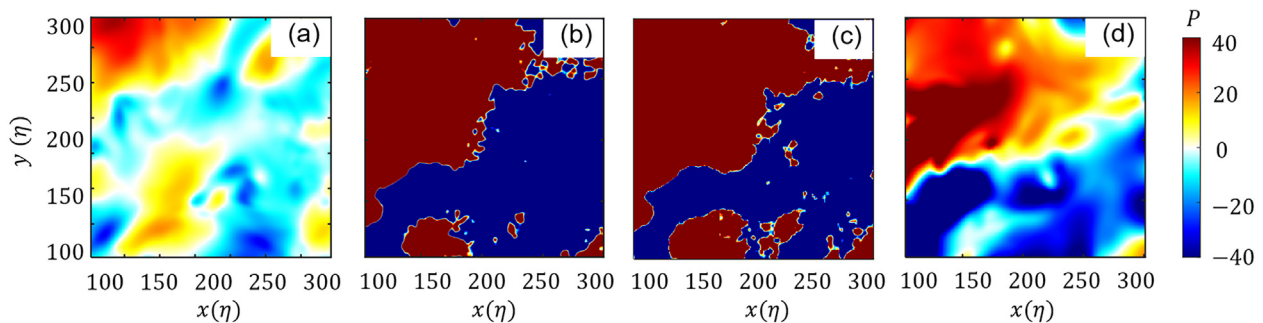


FIG. 6. Contours of pressure field (a) original DNS pressure field, (b) predicted by the SDFPI method, (c) predicted by IC-OPI, (d) predicted by PINN based on 2D2C PIV data.

From the visual comparison, all the reconstructed pressures present a large deviation from the DNS data. This is because the strong three-dimensionality of forced isotropic turbulence, i.e., the influence of velocity and velocity derivation in the third direction, which have the same order of magnitude as the x and y directions, cannot be ignored. Therefore, it is impossible to obtain a correct pressure field from planar PIV for three-dimensional flow, such as forced isotropic turbulence. In particular, because of the strong three-dimensionality of the flow, the pressure gradient possesses great errors in calculating the pressure, which causes that the results from SDFPI and IC-OPI appear similar under the current color scale. To fully assess the performance of pressure reconstruction, we construct 2D3C PIV velocity data from the same data set to evaluate the effect of three-dimensionality on PINN-based pressure reconstruction.

For the 2D3C velocity data, the DNS velocity fields are first smoothed using a moving average filtering with different integration window sizes. In the present work, interrogation windows with size of $15 \eta \times 15 \eta \times 15 \eta$, $30 \eta \times 30 \eta \times 30 \eta$, and $45 \eta \times 45 \eta \times 45 \eta$ are adopted to high, medium, and low resolution of the 2D3C data, respectively. Note that the velocity in the out-of-plane direction is also filtered. Then, the filtered data in the region of $100 \eta \leq x \leq 304 \eta$ and $100 \eta \leq y \leq 304 \eta$ is interpolated to the PIV mesh with a square spacing of half of the interrogation window, to simulate the 50% overlap. 500 x - y slices with three-component velocity data are generated for each case.

Note that a 3 D PINN was adopted to tackle the 2D3C PIV data. The computational domain in the x and y direction is the same as the PIV data, while, that in the z direction is four times the spacing of PIV and the data plane is placed at the middle of the z direction. Figure 7 shows the velocity and pressure reconstructed by PINN using high-resolution 2D3C PIV data. The flow fields reconstructed by PINN show good agreement with the reference DNS data. To validate the quality of reconstruction, the corresponding relative error is also shown in Fig. 8 for high, medium, and low resolution, respectively. The relative error is defined as $(X_p - X_{dns})/X_{ref}$, where the parameter X can be velocity components or pressure and X_{ref} is chose as the corresponding maximum absolute value of the DNS data (Wang et al., 2016). It is obvious that larger interrogation window (i.e., low resolution of PIV data) results in larger relative velocity and pressure error. From visual inspection of the results, we can conclude that PINN can correctly reconstruct the velocity and pressure from the high-resolution 2D3C PIV data.

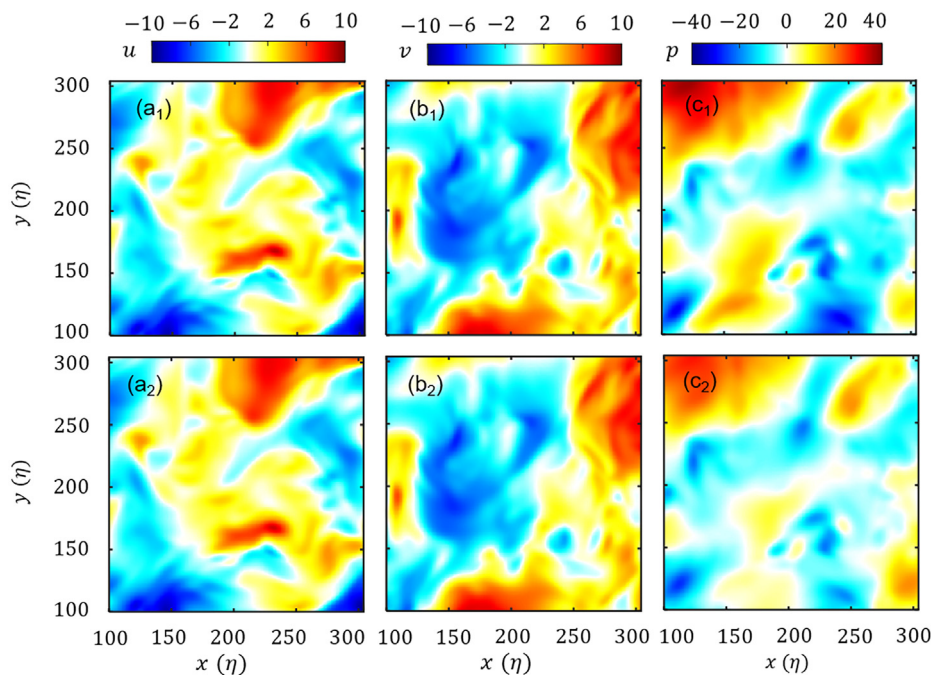


FIG. 7. (a₁) DNS streamwise velocity u field, (a₂) streamwise velocity u predicted by PINN; (b₁) DNS spanwise velocity v field, (b₂) spanwise velocity v predicted by PINN; (c₁) DNS pressure field, (c₂) pressure predicted by PINN using high-resolution 2D3C PIV data.

Table II quantitatively lists the relative L^2 norm error of streamwise velocity u , spanwise velocity v , and pressure p . When calculating relative L^2 norm error according to Eq. (8), the reference value is the corresponding DNS data. For the fields reconstructed by PINN using high resolution data, the relative L^2 norm error of velocity u is 1.33% and that of the pressure is 14.22%, and for the low resolution data, the relative L^2 norm error of velocity u is 2.56% and that of the pressure is 16.95%. The correlation coefficient R between the reconstructed field and the DNS field is also given in Table II. The correlation coefficient of velocity is approximately 0.99, and the correlation coefficient of pressure is smaller than 0.90.

From the above analysis, we present that the 2D2C PIV data cannot be used to correctly estimate the pressure for strong three-dimensional flow. The strategy of PINN with 2D3C data is feasible for pressure reconstruction. Meanwhile, the performance of PINN can benefit from improving the resolution of PIV data. The PTV data may be more suitable for PINN-based pressure reconstruction.

C. Synthetic jet impinging on a solid wall

In this section, the experimental PIV data of an impinging synthetic jet was used to evaluate the performance of different pressure reconstruction methods. The experiment was conducted in a large water tank. The synthetic jet was created from a piston-cylinder actuator with the exit diameter $D = 10$ mm. The jet Reynolds number was chosen as $Re_{sj} = 332$ at a driving frequency equaling $f_0 = 0.6$ Hz. A time-resolved planar PIV system was employed to measure the fluid velocity in the symmetric plane of the synthetic jet. The camera resolution was set to 1536×836 pixels, yielding a field of view of about 90×50 mm ($9D \times 5D$). The PIV interrogation window was set as 32×32 pixels with 75% overlap that results in a vector spacing of 0.47 mm approximately. Both the synthetic jet and PIV parameters are

summarized in Table III, and details of the experimental setup can be found in Xu *et al.* (2017). Note that considering the periodic nature of synthetic jets, the input velocity for the pressure reconstruction was the phase-averaged data with 400 snapshots in a period.

Since the PIV data were obtained at the symmetric plane of the synthetic jet, the two-dimensional N-S equations in cylindrical coordinates were used for the loss function of PINN. The PIV velocity field was first interpolated to a structured grid, and then, the pressure was calculated using all three methods, i.e., PINN, SDFPI, and IC-OPI. Note that in the PINN calculation, the neural network was set to 14 layers with 64 neurons in each layer, and the pressure result was extracted after 30 000 epochs when the loss was reduced to be less than 10^{-2} . For an axisymmetric flow and cylindrical coordinates, the difference of PPE between cylindrical and Cartesian coordinate is one or two orders of magnitude smaller than the PPE in Cartesian coordinate (Naguib and Koochesfahani, 2004); thus, SDFPI and IC-OPI are solved in Cartesian coordinate. In addition, to quantitatively show the effect of coordinate system selection, the pressure calculated by PINN using two-dimensional N-S equations in cylindrical coordinates and Cartesian coordinates is compared in Fig. 9. The average difference between pressures calculated using two coordinate systems is 0.8% at $t/T_0 = 0.2125$ and 2% at $t/T_0 = 0.35$ relative to their respective maximum, which is negligibly small. Therefore, we consider that using Cartesian coordinate is acceptable for a symmetric flow in Sec. III C.

The pressure fields computed by PINN, SDFPI, and IC-OPI are presented in Figs. 10(a)–10(c), respectively. Three time instants at $t/T_0 = 0.0625$, 0.2125, and 0.35 were chosen for comparison. As mentioned above, the IC-OPI and SDFPI is sensitive to both noise and boundary conditions; therefore, these two methods have worse performance on the experimental data. As illustrated in Figs. 10(c₁)–10(c₃), although the SDFPI and IC-OPI could present the basic pressure distribution associated with an impinging synthetic jet, i.e., low pressure

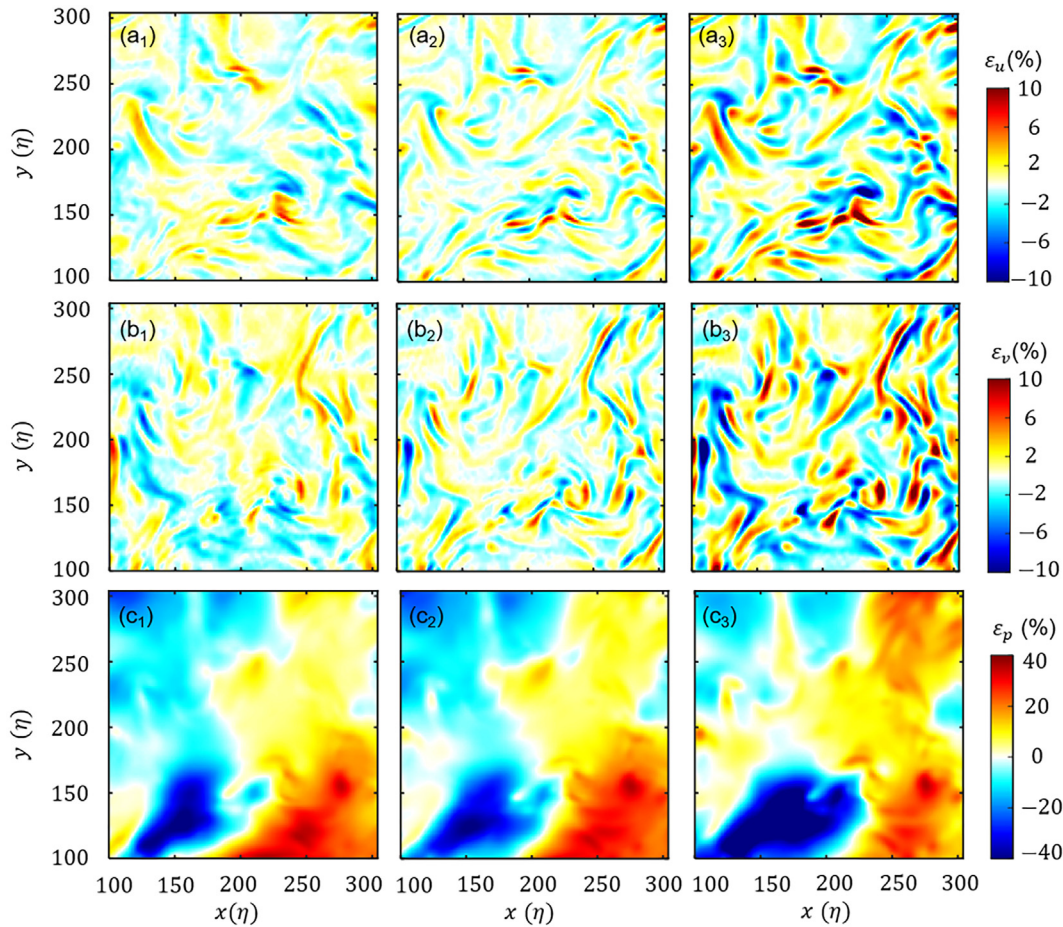


FIG. 8. (a₁)–(a₃) Relative streamwise velocity error ϵ_u , (b₁)–(b₃) relative spanwise velocity error ϵ_v , and (c₁)–(c₃) relative pressure error ϵ_p at input velocities with (a₁)–(c₁) high resolution, (a₂)–(c₂) medium resolution, and (a₃)–(c₃) low resolution.

TABLE II. Correlation coefficient and relative L^2 norm errors of velocity u , v , and pressure p , compared with DNS velocity and pressure field. 2D3C PIV data is generated as low, medium, and high resolution.

	u		v		p	
	R	$\delta_u(\%)$	R	$\delta_v(\%)$	R	$\delta_p(\%)$
High resolution	0.99	1.33	0.99	1.54	0.89	14.22
Medium resolution	0.99	1.29	0.99	1.55	0.89	14.51
Low resolution	0.99	2.56	0.99	3.05	0.84	16.95

at the vortex cores and high pressure at the impingement stagnation, its calculated pressure field is significantly contaminated by the measurement noise especially in quiescent surrounding fluid [see Figs. 10(b) and 10(c)]. Figure 10(a) shows that the pressure fields reconstructed from the PINN well resolve the vortex ring evolution of the impinging synthetic jet. This result indicates that the PINN possesses the best

TABLE III. Flow and PIV parameters for the impinging synthetic jet experiment.

Flow parameters	Exit diameter D	10 mm
	Orifice-to-wall distance H	40 mm
	Frequency of the synthetic jet f_0	0.6 Hz
	Reynolds number Re_{sj}	332
	Non-dimensional stroke length L/D	5.5
PIV parameters	Laser thickness	1 mm
	Laser power	5 W
	Camera resolution	1536 × 836 pixels
	Particle diameter	10 μm
	Interrogation window size	32 × 32 pixels
	Overlap ratio	75%
	Seeding particle density	~0.0527 ppp

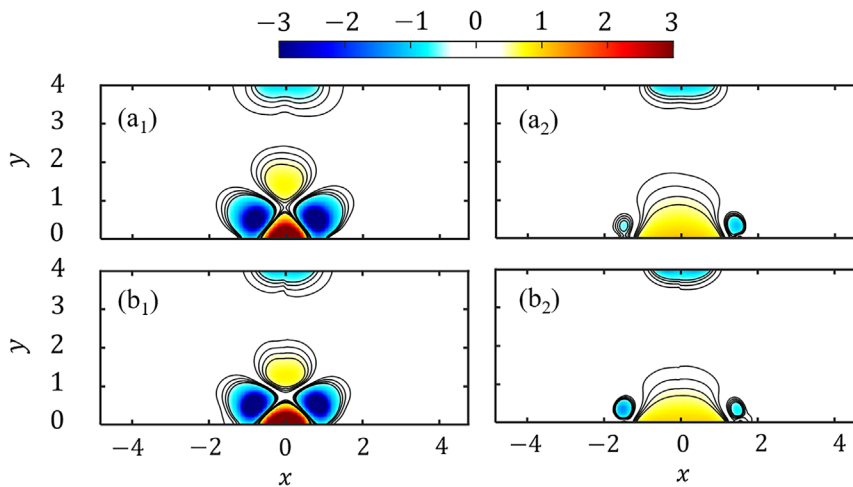


FIG. 9. Pressure field reconstructed by PINN using two-dimensional N-S equations in (a₁)–(a₂) Cartesian coordinates, and (b₁)–(b₂) cylindrical coordinates, when (a₁)–(b₁) $t/T_0 = 0.2125$, and (a₂)–(b₂) $t/T_0 = 0.35$.

performance in the pressure reconstruction and is minimally affected by the experimental noise among all three tested methods.

To illustrate the role of pressure in revealing the mechanism of flow dynamics, Fig. 11 shows the vorticity field and wall pressure distribution estimated from PINN. Three time instants at $t/T_0 = 0.0625$, 0.2125 , and 0.35 correspond to the vortex ring evolution before the impingement, impinging onto the wall and after the impingement, respectively. As shown in Figs. 11(a₁)–11(d₁), before impinging onto the wall, the fluid out of the jet orifice forms a vortex ring followed by a trailing jet. The vortex cores have a low-pressure region and, in its front and rear, generate high-pressure areas that are related to the leading and trailing stagnation points in a frame of reference moving with the ring (Lawson and Dawson, 2013). The wall pressure

distribution shows a peak at the jet centerline ($x = 0$), which indicates a possible early interaction with the wall.

As the vortex ring moves forward to impinge onto the wall at $t/T_0 = 0.2125$, a high-pressure area is formed around the wall stagnation point, and two pressure valleys appear near $x = \pm 1$ corresponding to the position of primary vortex cores, as shown in Figs. 11(b₂) and 11(c₂). The wall pressure distribution in Fig. 11(d₂) shows that the coefficient peak at the jet centerline experienced a significant increase compared to Figs. 11(d₁) and 11(d₃) due to the intensive vortex/wall interaction. In particular, following the pressure valleys ($x = \pm 1$), it seems that the flow would experience an adverse pressure gradient (APG) along the radial direction. This means that a potential flow separation could occur.

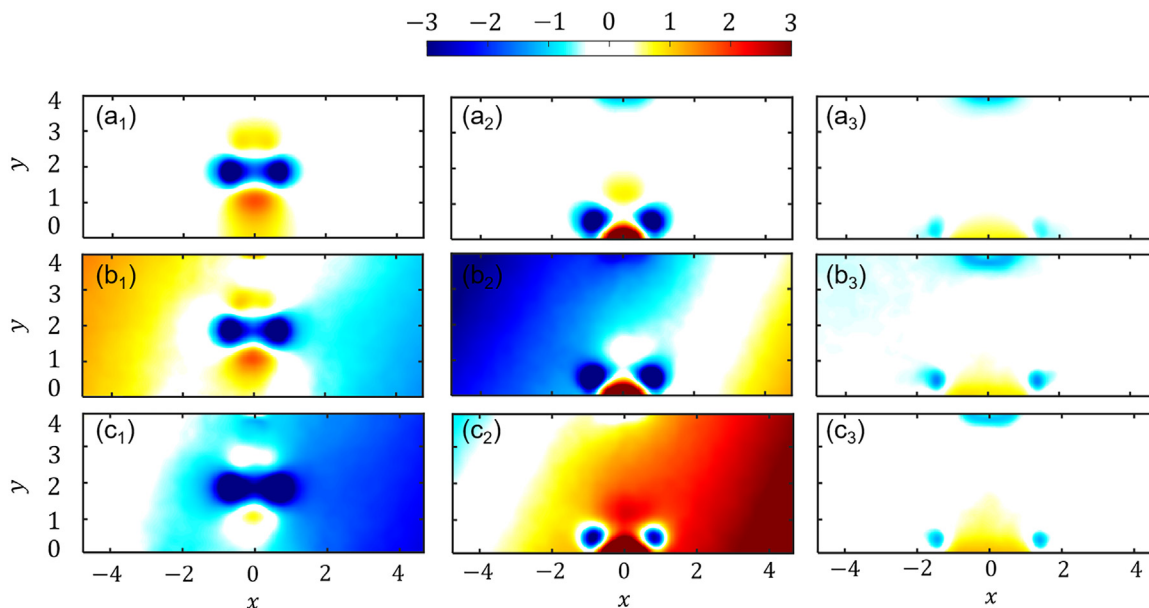


FIG. 10. Pressure field reconstructed by (a₁)–(a₃) PINN, (b₁)–(b₃) SDFPI, and (c₁)–(c₃) IC-OPI methods, when (a₁)–(c₁) $t/T_0 = 0.0625$, (a₂)–(c₂) $t/T_0 = 0.2125$, and (a₃)–(c₃) $t/T_0 = 0.35$.

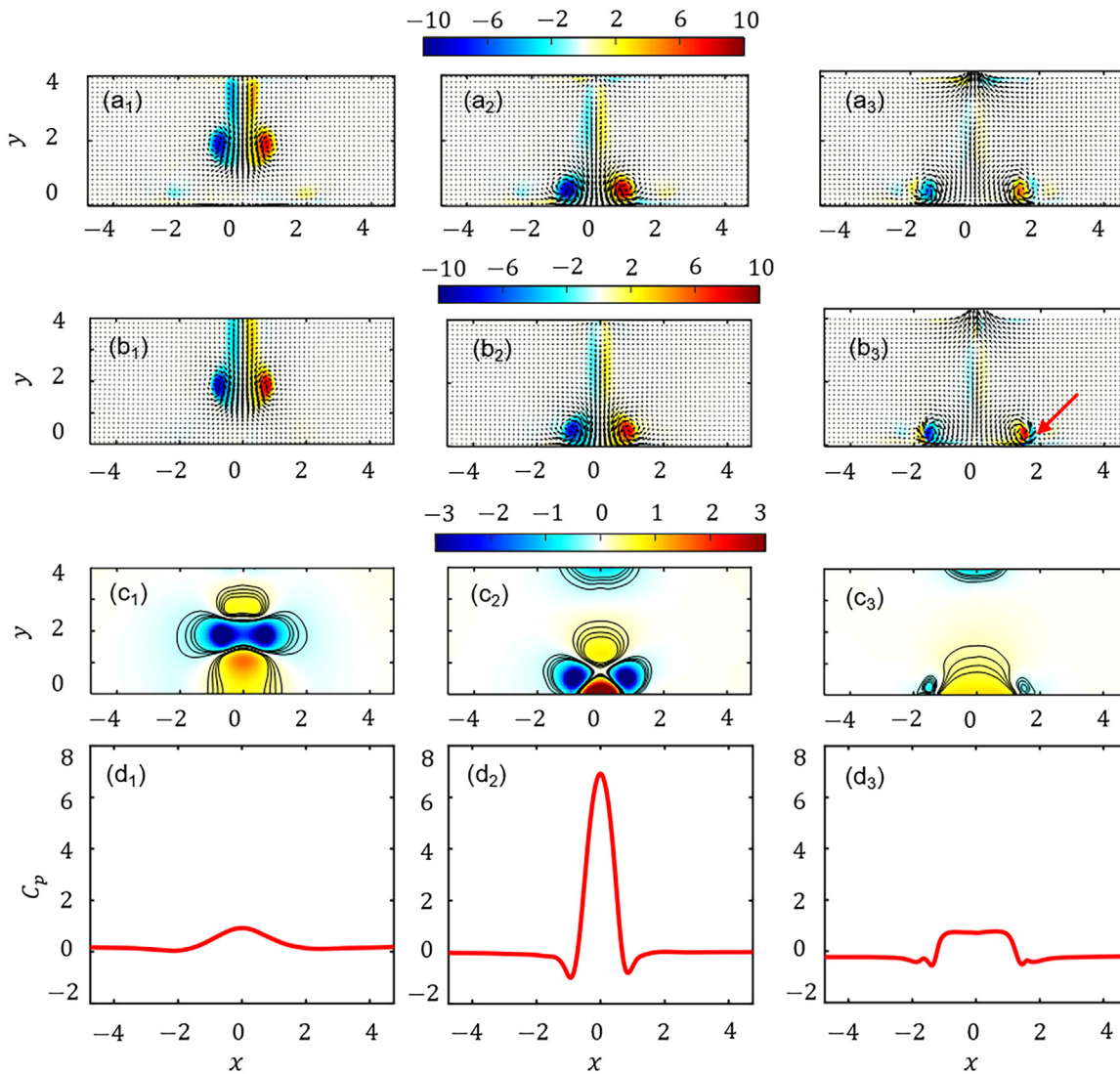


FIG. 11. (a₁)–(a₃) Vorticity field calculated by PIV data, (b₁)–(b₃) vorticity field calculated by velocity predicted by PINN, (c₁)–(c₃) pressure field reconstructed by PINN, and (d₁)–(d₃) pressure coefficient on the wall at $t = (a_1)-(d_1) 0.0625T_0$, $(a_2)-(d_2) 0.2125T_0$, and $(a_3)-(d_3) 0.35T_0$.

As time evolved to $t/T_0 = 0.35$, the primary vortex ring continues to interact with the wall to expand along the radial direction. During this process, both the stagnation peak and vortex core valleys in the pressure field had a significant reduction, as shown in Fig. 11(c₃). It was notable that in addition to the primary vortex core valley, a second pressure valley was detected in the wall pressure distribution, as shown in Fig. 11(d₃). This second valley was attributed to the secondary vortex ring formed from the separation of the wall shear layer induced by the impinging primary vortex ring, as pointed by red arrows in Fig. 11(b₃). Moreover, the wall pressure presents a plateau around the jet centerline, which was due to the impingement of the trailing jet following the primary vortex ring. In general, for other complex flows and for those which is difficult to measure the pressure field, the PINN can help to reconstruct the pressure field, which is beneficial for in-

depth analysis of complex flow phenomena, such as the evolution of a vortex/wall interaction shown in the current case.

IV. CONCLUSION

Unlike traditional methods of pressure reconstruction, i.e., SDFPI and IC-OPI, PINN can simultaneously optimize the PIV velocity and predict the pressure. PINN combines the laws of physics with traditional pure data-driven neural networks to calculate unknown pressure by minimizing the total loss including equation loss and data loss. In this work, the performance of PINN is numerically investigated using two-dimensional Taylor’s decaying vortices, forced isotropic turbulence, and then an experiment involving a synthetic jet impinging on a solid wall is used to test the pressure-reconstruction ability of PINN for noisy PIV data. This work produced several outcomes.

First, compared to traditional methods, PINN reconstructs pressure fields with the lowest relative pressure error even the input velocity field is contaminated by noise. This is because PINN can optimize the velocity by imposing the physical constraint. Using the optimized velocity fields, the traditional methods can also get better pressure fields. Meanwhile, increasing N_{cell} , N_{data} and N_{eqns} can reduce pressure error, and the influence of N_{data} is greater than the influence of N_{eqns} . This implies that the performance of PINN-based pressure reconstruction can be improved by increasing the quantity of the measured data.

Second, for three-dimensional flow, such as forced homogeneous isotropic turbulence, the pressure cannot be recovered from 2D2C velocity fields even for the proposed PINN. However, a 3D PINN has the capability to reconstruct the pressure from 2D3C velocity fields. The modulation effect introduced by the cross correlation algorithm in PIV deteriorates the performance of PINN; therefore, data with high resolution and low noise can increase the accuracy of pressure reconstruction.

Finally, two-dimensional PIV experimental data are used to test pressure reconstruction performance. For complex nonperiodic turbulence flow, traditional methods meet many problems such as conflicting with N-S equations constraints when reconstructing a pressure field. However, PINN can accurately predict the complex flow structure, such as a secondary vortex, which is hard to observe in experimental measurements and is meaningful for understanding the flow structure evolution of a synthetic impinging jet. From the pressure field reconstructed by PINN, more information about the flow mechanism, such as the pressure coefficient, is correctly obtained, which is important for analyzing complex physical phenomena.

Herein, compared to traditional methods, PINN can reconstruct pressure fields with high accuracy and reduce the influence of velocity noise when PIV data are contaminated by noise. However, choosing suitable parameters for PINN is critical and time-consuming. Further investigation on the possibility of saving calculation time is also needed.

ACKNOWLEDGMENTS

This work was financially supported by the National Natural Science Foundation of China (NSFC, Grant Nos. 11902019, 12172030, and 12072348) and the Fundamental Research Funds for the Central Universities.

AUTHOR DECLARATIONS

Conflict of Interest

The authors have no conflicts to disclose.

Author Contributions

Di Fan: Data curation (equal); Formal analysis (equal); Visualization (equal); Writing – original draft (equal). **Yang Xu:** Conceptualization (equal); Funding acquisition (equal); Project administration (equal); Supervision (equal); Validation (equal); Writing – review & editing (equal). **Hongping Wang:** Conceptualization (equal); Funding acquisition (equal); Methodology (equal); Resources (equal); Software (equal); Supervision (equal); Validation (equal); Visualization (equal); Writing – review & editing (equal). **Jin-Jun Wang:** Funding acquisition (equal); Supervision (equal).

DATA AVAILABILITY

The data that support the findings of this study are available from the corresponding author upon reasonable request.

REFERENCES

- Arzani, A., Wang, J. X., and D'Souza, R. M., "Uncovering near-wall blood flow from sparse data with physics-informed neural networks," *Phys. Fluids* **33**, 071905 (2021).
- Bach, J. S. and Bruus, H., "Theory of pressure acoustics with viscous boundary layers and streaming in curved elastic cavities," *J. Acoust. Soc. Am.* **144**(2), 766–784 (2018).
- Buxton, O. R. H., Laizet, S., and Ganapathisubramani, B., "The effects of resolution and noise on kinematic features of fine-scale turbulence," *Exp. Fluids* **51**(5), 1417–1437 (2011).
- Cai, Z. M., Liu, Y., Chen, T., and Liu, T. S., "Variational method for determining pressure from velocity in two dimensions," *Exp. Fluids* **61**, 118 (2020).
- Calicchia, M. A., Mittal, R., Seo, J. H., and Ni, R., "Reconstructing the pressure field around swimming fish using a physics-informed neural network," *J. Exp. Biol.* **226**, jeb244983 (2023).
- Charonko, J. J., King, C. V., Smith, B. L., and Vlachos, P. P., "Assessment of pressure field calculations from particle image velocimetry measurements," *Meas. Sci. Technol.* **21**, 105401 (2010).
- Dabiri, J. O., Bose, S., Gemmill, B. J., Colin, S. P., and Costello, J. H., "An algorithm to estimate unsteady and quasi-steady pressure fields from velocity field measurements," *J. Exp. Biol.* **217**(3), 331–336 (2014).
- de Kat, R. and van Oudheusden, B. W., "Instantaneous planar pressure determination from PIV in turbulent flow," *Exp. Fluids* **52**(5), 1089–1106 (2012).
- Du, M. Y., Zhang, C., Xie, S., Pu, F., Zhang, D., and Li, D. Y., "Investigation on aortic hemodynamics based on physics-informed neural network," *Math. Biosci. Eng.* **20**(7), 11545–11567 (2023).
- Elliott, J. A., "Microscale pressure fluctuations measured within the lower atmospheric boundary layer," *J. Fluid Mech.* **53**(2), 351–384 (1972).
- Ethier, C. R. and Steinman, D. A., "Exact fully 3D Navier–Stokes solutions for benchmarking," *Int. J. Numer. Methods Fluids* **19**, 369–375 (1994).
- Faiella, M., Grant Jeon Macmillan, C., Whitehead, J. P., and Pan, Z., "Error propagation dynamics of velocimetry-based pressure field calculations (2): On the error profile," *Meas. Sci. Technol.* **32**, 084005 (2021).
- Fujisawa, N., Nakamura, Y., Matsuura, F., and Sato, Y., "Pressure field evaluation in microchannel junction flows through mu PIV measurement," *Microfluid. Nanofluid.* **2**(5), 447–453 (2006).
- Gunaydinoglu, E. and Kurtulus, D. F., "Pressure–velocity coupling algorithm-based pressure reconstruction from PIV for laminar flows," *Exp. Fluids* **61**, 5 (2020).
- Karniadakis, G. E., Kevrekidis, I. G., Lu, L., Perdikaris, P., Wang, S. F., and Yang, L., "Physics-informed machine learning," *Nat. Rev. Phys.* **3**(6), 422–440 (2021).
- Kim, J. and Moin, P., "Application of a fractional-step method to incompressible Navier–Stokes equations," *J. Comput. Phys.* **59**(2), 308–323 (1985).
- Kimura, F., McCann, J., Khalil, G. E., Dabiri, D., Xia, Y. N., and Callis, J. B., "Simultaneous velocity and pressure measurements using luminescent microspheres," *Rev. Sci. Instrum.* **81**, 064101 (2010).
- Klein, C., Engler, R. H., Henne, U., and Sachs, W. E., "Application of pressure-sensitive paint for determination of the pressure field and calculation of the forces and moments of models in a wind tunnel," *Exp. Fluids* **39**(2), 475–483 (2005).
- Kurose, R. and Komori, S., "Drag and lift forces on a rotating sphere in a linear shear flow," *J. Fluid Mech.* **384**, 183–206 (1999).
- Lawson, J. M. and Dawson, J. R., "The formation of turbulent vortex rings by synthetic jets," *Phys. Fluids* **25**, 105113 (2013).
- Lee, I., Ahn, S. K., and Sung, H. J., "Three-dimensional coherent structure in a separated and reattaching flow over a backward-facing step," *Exp. Fluids* **36**(3), 373–383 (2004).
- Li, Y., Perlman, E., Wan, M. P., Yang, Y. K., Meneveau, C., Burns, R., Chen, S. Y., Szalay, A., and Eyink, G., "A public turbulence database cluster and applications to study Lagrangian evolution of velocity increments in turbulence," *J. Turbul.* **9**(31), N31 (2008).

- Liu, X. F. and Katz, J., “Instantaneous pressure and material acceleration measurements using a four-exposure PIV system,” *Exp. Fluids* **41**(2), 227–240 (2006).
- Liu, X. F. and Moreto, J. R., “Error propagation from the PIV-based pressure gradient to the integrated pressure by the omnidirectional integration method,” *Meas. Sci. Technol.* **31**, 055301 (2020).
- Mao, Z. P., Jagtap, A. D., and Karniadakis, G. E., “Physics-informed neural networks for high-speed flows,” *Comput. Method Appl. Mech. Eng.* **360**, 112789 (2020).
- McClure, J. and Yarusevych, S., “Optimization of planar PIV-based pressure estimates in laminar and turbulent wakes,” *Exp. Fluids* **58**, 62 (2017).
- McLachlan, B. G., Kavandi, J. L., Callis, J. B., Gouterman, M., Green, E., Khalil, G., and Burns, D., “Surface pressure field mapping using luminescent coatings,” *Exp. Fluids* **14**(1), 33–41 (1993).
- Moreto, J. R., Reeder, W. J., Budwig, R., Tonina, D., and Liu, X. F., “Experimentally mapping water surface elevation, velocity, and pressure fields of an open channel flow around a stalk,” *Geophys. Res. Lett.* **49**, e2021GL096835, <https://doi.org/10.1029/2021GL096835> (2022).
- Naguib, A. M. and Koochesfahani, M. M., “On wall-pressure sources associated with the unsteady separation in a vortex-ring/wall interaction,” *Phys. Fluids* **16**(7), 2613–2622 (2004).
- Nie, M. Y., Whitehead, J. P., Richards, G., Smith, B. L., and Pan, Z., “Error propagation dynamics of PIV-based pressure field calculation (3): What is the minimum resolvable pressure in a reconstructed field?,” *Exp. Fluids* **63**, 168 (2022).
- Pan, Z., Whitehead, J., Thomson, S., and Truscott, T., “Error propagation dynamics of PIV-based pressure field calculations: How well does the pressure Poisson solver perform inherently?,” *Meas. Sci. Technol.* **27**, 084012 (2016).
- Qiu, R. D., Huang, R. F., Xiao, Y., Wang, J. Z., Zhang, Z., Yue, J. S., Zeng, Z., and Wang, Y. W., “Physics-informed neural networks for phase-field method in two-phase flow,” *Phys. Fluids* **34**, 052109 (2022).
- Raissi, M., Perdikaris, P., and Karniadakis, G. E., “Physics informed deep learning (Part I): Data-driven solutions of nonlinear partial differential equations,” [arXiv:1711.10561](https://arxiv.org/abs/1711.10561) (2017a).
- Raissi, M., Perdikaris, P., and Karniadakis, G. E., “Physics informed deep learning (Part II): Data-driven discovery of nonlinear partial differential equations,” [arXiv:1711.10566](https://arxiv.org/abs/1711.10566) (2017b).
- Raissi, M., Perdikaris, P., and Karniadakis, G. E., “Physics-informed neural networks: A deep learning framework for solving forward and inverse problems involving nonlinear partial differential equations,” *J. Comput. Phys.* **378**, 686–707 (2019).
- Raissi, M., Yazdani, A., and Karniadakis, G. E., “Hidden fluid mechanics: Learning velocity and pressure fields from flow visualizations,” *Science* **367**(6481), 1026–1030 (2020).
- Rubinow, S. I. and Keller, J. B., “The transverse force on a spinning sphere moving in a viscous fluid,” *J. Fluid Mech.* **11**(3), 447–459 (1961).
- Saffman, P. G., “The lift on a small sphere in a slow shear flow,” *J. Fluid Mech.* **22**(2), 385–400 (1965).
- Schiassi, E., De Florio, M., Ganapol, B. D., Picca, P., and Furfaro, R., “Physics-informed neural networks for the point kinetics equations for nuclear reactor dynamics,” *Ann. Nucl. Energy* **167**, 108833 (2022).
- Tsuji, Y., Fransson, J. H. M., Alfredsson, P. H., and Johansson, A. V., “Pressure statistics and their scaling in high-Reynolds-number turbulent boundary layers,” *J. Fluid Mech.* **585**, 1–40 (2007).
- Vadyala, S. R., Betgeri, S. N., and Betgeri, N. P., “Physics-informed neural network method for solving one-dimensional advection equation using PyTorch,” *Array* **13**, 100110 (2022).
- van Gent, P. L., Michaelis, D., van Oudheusden, B. W., Weiss, P. É., de Kat, R., Laskari, A., Jeon, Y. J., David, L., Schanz, D., Huhn, F., Gesemann, S., Novara, M., McPhaden, C., Neeteson, N. J., Rival, D. E., Schneiders, J. F. G., and Schrijer, F. F. J., “Comparative assessment of pressure field reconstructions from particle image velocimetry measurements and Lagrangian particle tracking,” *Exp. Fluids* **58**, 33 (2017).
- van Oudheusden, B. W., “PIV-based pressure measurement,” *Meas. Sci. Technol.* **24**, 032001 (2013).
- Voskoboinick, V., Kornev, N., and Turnow, J., “Study of near wall coherent flow structures on dimpled surfaces using unsteady pressure measurements,” *Flow, Turbul. Combust.* **90**(4), 709–722 (2013).
- Wang, C. Y., Gao, Q., Wei, R. J., Li, T., and Wang, J. J., “Spectral decomposition-based fast pressure integration algorithm,” *Exp. Fluids* **58**, 84 (2017).
- Wang, H. P., Liu, Y., and Wang, S. Z., “Dense velocity reconstruction from particle image velocimetry/particle tracking velocimetry using a physics-informed neural network,” *Phys. Fluids* **34**, 017116 (2022).
- Wang, Z. Y., Gao, Q., Wang, C. Y., Wei, R. J., and Wang, J. J., “An irrotation correction on pressure gradient and orthogonal-path integration for PIV-based pressure reconstruction,” *Exp. Fluids* **57**, 104 (2016).
- Wu, G. Z., Fang, Y., Kudryashov, N. A., Wang, Y. Y., and Dai, C. Q., “Prediction of optical solitons using an improved physics-informed neural network method with the conservation law constraint,” *Chaos, Solitons Fractals* **159**, 112143 (2022).
- Xie, J. B., Chai, Z., Xu, L. M., Ren, X. K., Liu, S., and Chen, X. Q., “3D temperature field prediction in direct energy deposition of metals using physics informed neural network,” *Int. J. Adv. Manuf. Technol.* **119**, 3449–3468 (2022).
- Xu, Y., He, G. S., Kulkarni, V., and Wang, J. J., “Experimental investigation of influence of Reynolds number on synthetic jet vortex rings impinging onto a solid wall,” *Exp. Fluids* **58**, 6 (2017).
- Zhang, J. C., Bhattacharya, S., and Vlachos, P. P., “Uncertainty of PIV/PTV based Eulerian pressure estimation using velocity uncertainty,” *Meas. Sci. Technol.* **33**, 065303 (2022).